# Accepted Manuscript

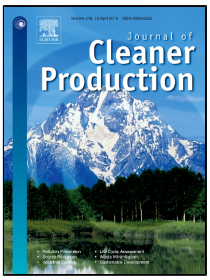


Linking the $SO_2$ emission of cement plants to the sulfur characteristics of their limestones: A study of 80 NSP cement lines in China

Tongsheng Zhang, Chang Wu, Bin Li, Jiawei Wang, Rasheeda Ravat, Xinzhi Chen, Jiangxiong Wei, Qijun Yu

| | |
|---|---|
| PII: | S0959-6526(19)30522-0 |
| DOI: | 10.1016/j.jclepro.2019.02.133 |
| Reference: | JCLP 15863 |
| To appear in: | *Journal of Cleaner Production* |
| Received Date: | 04 September 2018 |
| Accepted Date: | 13 February 2019 |

Please cite this article as: Tongsheng Zhang, Chang Wu, Bin Li, Jiawei Wang, Rasheeda Ravat, Xinzhi Chen, Jiangxiong Wei, Qijun Yu, Linking the $SO_2$ emission of cement plants to the sulfur characteristics of their limestones: A study of 80 NSP cement lines in China, *Journal of Cleaner Production* (2019), doi: 10.1016/j.jclepro.2019.02.133

# Linking the $SO_2$ emission of cement plants to the sulfur characteristics of their limestones: A study of 80 NSP cement lines in China

Tongsheng Zhang[a,b*], Chang Wu[a], Bin Li[a], Jiawei Wang[c], Rasheeda Ravat[c], Xinzhi Chen[d], Jiangxiong Wei[a], Qijun Yu[a*]

[a] School of Materials Science and Engineering, South China University of Technology, 510640 Guangzhou, China

[b] Department of Civil, Environmental and Geomatic Engineering, University College London, WC1E 6BT, UK

[c] School of Engineering and Applied Science, Aston University, Aston Triangle, B4 7ET Birmingham, UK

[d] Guangdong Wanyin Technology Development Co. Ltd, 510075 Guangzhou, China

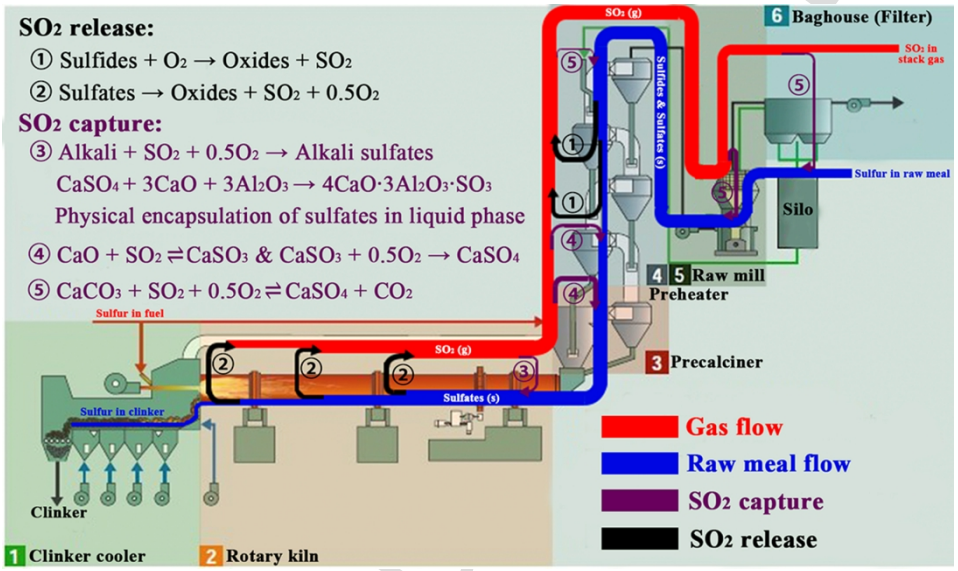


* Corresponding author. E-mail address: mstszhang@scut.edu.cn (Tongsheng Zhang), concyuq@scut.edu.cn (Qijun Yu). Tel./fax.: +86-020-87114233.

# Linking the $SO_2$ emission of cement plants to the sulfur characteristics of their limestones: A study of 80 NSP cement lines in China

Tongsheng Zhang[a,b*], Chang Wu[a], Bin Li[a], Jiawei Wang[c], Rasheeda Ravat[c], Xinzhi Chen[d], Jiangxiong Wei[a], Qijun Yu[a*]

[a] School of Materials Science and Engineering, South China University of Technology, 510640 Guangzhou, China

[b] Department of Civil, Environmental and Geomatic Engineering, University College London, WC1E 6BT, UK

[c] School of Engineering and Applied Science, Aston University, Aston Triangle, B4 7ET Birmingham, UK

[d] Guangdong Wanyin Technology Development Co. Ltd, 510075 Guangzhou, China

**Abstract:** In a properly operated new suspension preheater (NSP) cement line, the $SO_2$ emission is mainly originated from sulfides in the raw meal, and limestone, occupying about 85% wt. of the raw meal, is the dominant sulfur source. However, the sulfur characteristics of limestones and then their influences on the $SO_2$ emission have not been clarified yet. In the present study, 80 NSP cement lines with $SO_2$ emission > 200 mg/Nm$^3$ were recorded, the sulfur content and species as well as pyrite morphology of limestones were analyzed and then correlated to their resulting $SO_2$ emission. The results show that the $SO_2$ emission of stack gas increases linearly with the $SO_3$ content of limestone used, and sulfates lead to a 50% reduction in $SO_2$ emission relative to sulfides. Compared with average $SO_2$ emission, euhedral pyrite leads to a slightly higher $SO_2$ emission, whereas metasomatic pyrite results in a lower $SO_2$ emission, which can be attributed to the effects of accompanying elements (Ti, F, K, and Al etc.) on the desulfurization reaction and clinkerization in the whole NSP cement line. The relationships proposed can be used to predict the $SO_2$ emission based on the sulfur characteristics of limestone and to rationally utilize high-sulfur limestone in cement industry.

* Corresponding author. E-mail address: mstszhang@scut.edu.cn (Tongsheng Zhang), concyuq@scut.edu.cn (Qijun Yu). Tel./fax.: +86-020-87114237.

**Key words:** $SO_2$ emission; Sulfur characteristics; Limestone; NSP cement line; Pyrite

## 1. Introduction

In recent years, more than 60% of cities in China are suffering from serious air pollution, such as smog and acid rain. The number of smog days per year exceeds 50, in the larger cities it can even reach 100 days (China5e, 2014). Heavy acid rain is also very serious in the southern and eastern parts of China, and acid rain control area (the pH value of rainfall < 4.5) accounts for 8.4% of the total land area (Chen and Mulder, 2007). For instance, the PM 2.5 concentration of central and northeast parts of China was as high as 150 μg/m$^3$ in Dec. 2016, Hebei, Henan, Shandong provinces had a PM 2.5 concentration even higher than 300 μg/m$^3$ as shown in Fig. 1a (Fei123, 2017). Furthermore, the acid rain proportion of central and east parts of China is in the range of 50-75% (Fig. 1b), rainfalls with pH value of 3.5 have been reported in Hunan and Guangdong provinces (China gateway to corrosion and protection, 2011). Compared with acid rain in developed countries, acid rain in China has a higher concentration of $SO_4^{2-}$ and a lower concentration of $NO_3^-$, indicating that it is mainly attributed to industrial $SO_2$ emissions (Lei et al., 2011; Zhang et al., 2015). $SO_2$ is oxidized into $SO_3$ after escaping from stack, and then absorbed by moisture or droplets in the clouds to form sulfuric acid. Available particulate matter in the air may also be involved to form sulfate aerosols, which provide sites for further accumulation of particulate matter. Therefore, $SO_2$ emission results either in acid rain or smog, leading to the acidification of surface soil and water, reduction of biodiversity, and deterioration of human and animal health (Lee et al., 2003; Hajat et al., 2002), as evidenced in the Meuse Valley smog (1930), Donora smog (1948), London Great

smog (1952), and Harbin smog (2013).

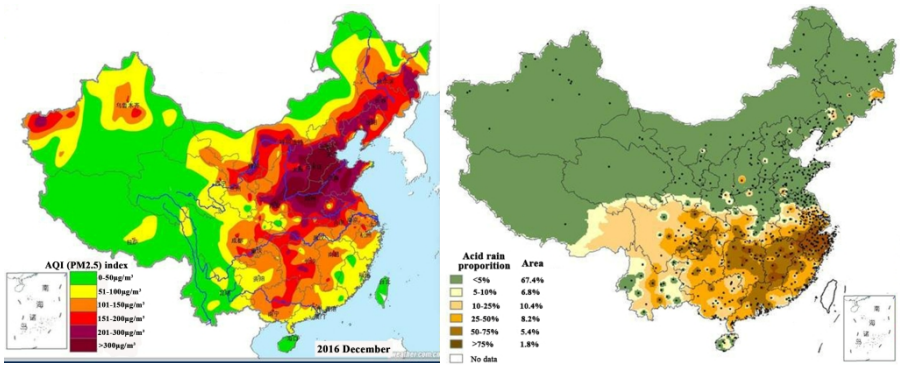


(a) Smog distribution (Fei123, 2017) (b) Acid rain distribution (China corrosion and protection, 2011)

Fig. 1 The smog and acid rain distributions in China, 2016

### 1.1 The $SO_2$ emission from Chinese cement industry

According to the data from the National Bureau of Statistics (MEEPC, 2016), the total $SO_2$ emission of China in 2015 is 18.6 million tons, and cement industry, the third largest $SO_2$ source, contributes to 1.47 million tons of $SO_2$ (about 8.7 %). Although the $SO_2$ emission from the cement industry increases gradually from 1990 to 2015 (Fig. 2a) due to the significant increase in the annual output of both clinker and cement, the $SO_2$ emission per ton of clinker decreases from 2.45 kg/t in 2000 to 1.12 kg/t in 2010, since the proportion of new suspension preheater (NSP) cement line increases from 10.3% in 2000 to 81.6% in 2010 as shown in Fig. 2b (Shen et al., 2017). In recent years, with limited availability and excessive costs of low-sulfur raw materials and fuels, high-sulfur raw materials and fuels have therefore been more and more utilized in Chinese cement plants. As a result, the sulfur input of the NSP cement lines increases gradually, followed by the $SO_2$ emission per ton of clinker up to 1.21 kg/t in 2016.

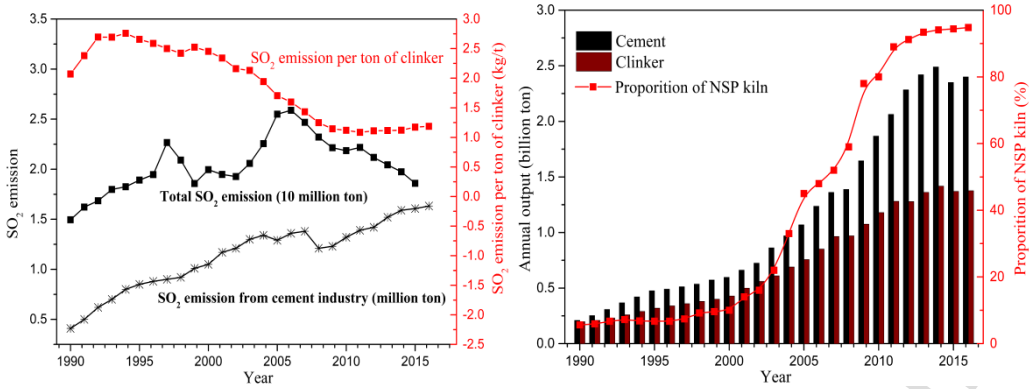


（a）$SO_2$ emission （b）Annual output of cement and clinker

Fig. 2 The $SO_2$ emission and annual output of Chinese cement industry, modified from (Shen et al., 2017)

Chinese government have identified $SO_2$ emission as a high-priority environmental problem that must be addressed immediately. In the national thirteenth "Five-Year Plan", the cement industry has been listed as a key industry for $SO_2$ emission reduction, to reduce or eliminate smog, acid rain and other pollutions. In 2013, national standard "Emission Standard of Air Pollutants for Cement Industry" (Chinese Standard, GB 4915-2013) was issued by the Ministry of Environmental Protection, the upper limitation of $SO_2$ in stack gas is 200 mg/Nm$^3$ for all cement lines in China, and stricter standards were further proposed by provincial governments. For instance, the upper limitation of $SO_2$ is 100 mg/Nm$^3$ for cement lines located in Guangdong, Shandong, Henan, and Fujian provinces, and only 20 mg/Nm$^3$、50 mg/Nm$^3$ for cement plants in Beijing and Hebei province, respectively.

### 1.2 The release and capture of $SO_2$ in NSP cement line

In a typical NSP cement line, 40~70% of $SO_2$ is released in the preheater due to the oxidization of sulfides and organic sulfur in raw meal, while the rest $SO_2$ is released in the precalciner and kiln due to the oxidization of sulfides and organic sulfur in fuel and the decomposition of sulfates from both raw

meal and fuel (Gossman, 2011). Since the raw mill, preheater, and precalciner use kiln exhaust gas to dry, heat and calcine the raw meal before it enters the kiln, the counter flow of raw meal and exhaust gas in the raw mill and preheater acts as inherent semi-dry (raw mill) and dry (preheater) scrubbers to control $SO_2$ emissions, and some $SO_2$ may also be dry scrubbed in the baghouse particulate control system (Helge, 2012; Horkoss, 2008). Therefore, the release and capture of $SO_2$ occur simultaneously as summarized in Table 1. It should be noted that the raw mill and preheater present low $SO_2$ capture capacity as the reaction rate between $SO_2$ and $CaCO_3$ is very slow (Ávila et al., 2005; Rasmussen, 2012). In contact, a large amount of CaO is available in the precalciner and the reaction rate between $SO_2$ and CaO is relatively higher, therefore most of $SO_2$ can be captured when flue gas passes through the precalciner (Shi et al., 2004; Hu, 2007). In addition, $SO_2$ can be also be absorbed by alkali and CaO in the kiln, however, 40-60% of the main desulfurization product, $CaSO_4$, will decompose and release $SO_2$ again during clinkerization.

Fig. 3 shows a simplified schematic sulfur flow in a NSP cement line (Mut et al., 2015). Desulfurization products, in terms of $CaSO_3$ and $CaSO_4$, either pass directly with the raw meal to the kiln or are collected by the baghouse particulate control system and then recirculated back into the raw meal. Thus, two sulfur cycles can be observed in a NSP cement line. One is the kiln-precalciner sulfur cycle. A large proportion of $SO_2$ released from sulfates decomposition in the kiln is captured by CaO in the precalciner and then returns back to the kiln. The second cycle is the preheater-raw mill/baghouse sulfur cycle. Sulfides in the raw meal oxide and release $SO_2$ in the C2/C3 cyclones, a small proportion

of $SO_2$ is consequently captured by $CaCO_3$ when the flue gas goes through the upper cyclones, raw mill, and baghouse. In a properly operated NSP cement line with a reasonable alkali-sulfur balance, $SO_2$ originated from fuel can be solidified into the clinker, as nearly all $SO_2$ passing through the precalciner is captured by the CaO generated. As a result, the concentration of $SO_2$ in the precalciner is very low as shown in Fig. 4 (Rasmussen, 2012; Hansen et al., 2003). The sulfur from the raw meal, however, is split, some exist within clinker and the rest in stack emission. Thus, the $SO_2$ emission in stack gas is originated mainly from sulfides in raw meal.

Table 1 The $SO_2$ release and capture in a typical NSP cement line (Gossman, 2011; Horkoss, 2008)

| Location | Temperature range | Sulfur source | $SO_2$ release | $SO_2$ capture |
|---|---|---|---|---|
| Raw mill<br>Bag house | 80~300℃ | — | — | $CaCO_3 + SO_2 + ½ O_2 \rightleftharpoons CaSO_4 + CO_2$ |
| Preheater | 300~880℃ | Organic S (Raw meal)<br>Sulfides (Raw meal) | Sulfides + $O_2 \rightarrow$ Oxides + $SO_2$<br>Organic S + $O_2 \rightarrow SO_2$ | $CaCO_3 + SO_2 + ½ O_2 \rightleftharpoons CaSO_4 + CO_2$ |
| Precalciner | 880~1000℃ | Organic S (Fuel)<br>Sulfides (Fuel) | Fuel S + $O_2 \rightarrow SO_2$<br>Sulfides + $O_2 \rightarrow$ Oxides + $SO_2$ | $CaO + SO_2 \rightleftharpoons CaSO_3$<br>$CaSO_3 + ½ O_2 \rightarrow CaSO_4$ |
| Kiln | 1000~1450℃ | Organic S (Fuel)<br>Sulfides (Fuel)<br>Sulfides (Raw meal, Fuel) | Fuel S + $O_2 \rightarrow SO_2$<br>Sulfides + $O_2 \rightarrow$ Oxides + $SO_2$<br>Sulfates $\rightarrow$ Oxides + $SO_2$ + ½ $O_2$<br>$CaSO_4 \rightarrow CaO + SO_2 + ½ O_2$ | $Na_2O + SO_2 + ½ O_2 \rightarrow Na_2SO_4$<br>$K_2O + SO_2 + ½ O_2 \rightarrow K_2SO_4$<br>$CaO + SO_2 + ½ O_2 \rightleftharpoons CaSO_4$<br>$CaSO_3 + ½ O_2 \rightarrow CaSO_4$ |

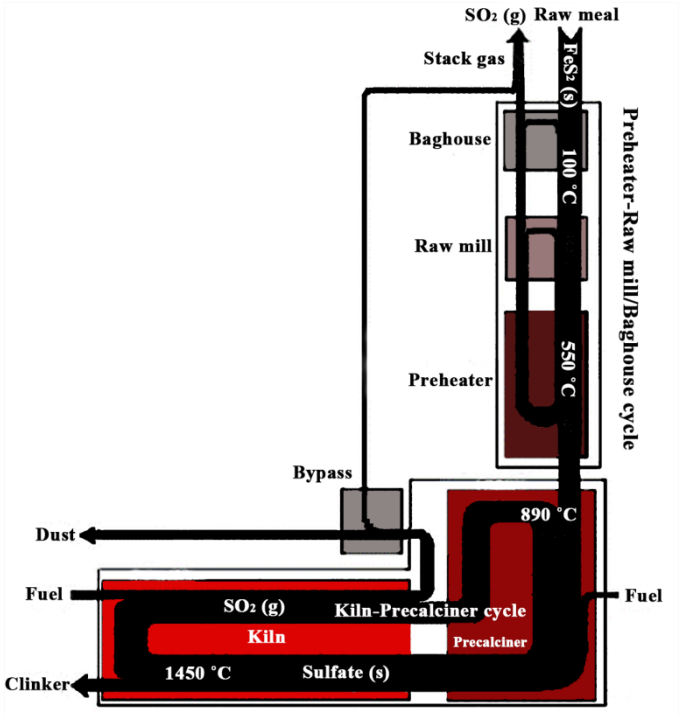


Fig. 3 Schematic sulfur flow in a typical NSP cement line (Mut et al., 2015)

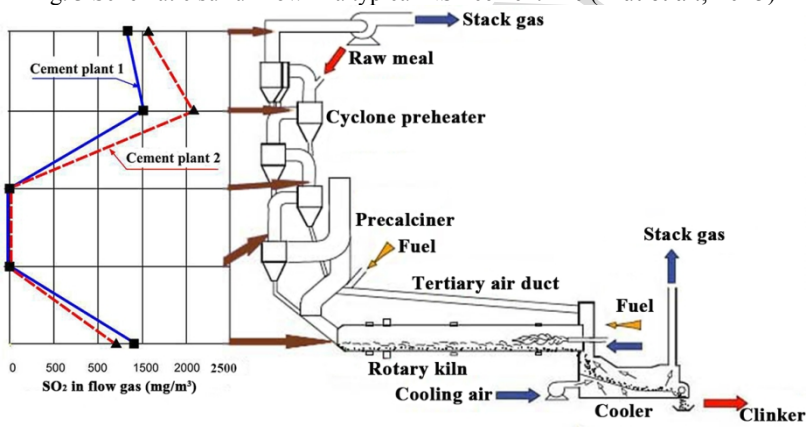


Fig. 4 The $SO_2$ concentration of flue gas at different locations of a typical NSP cement line (Hansen et al., 2003)

### 1.3 The sulfur-containing minerals in fuel and raw materials

Sulfur in raw meal and fuel can be classified into organic and inorganic sulfurs, and the later mainly refers to sulfides (such as pyrite) and sulfates (in terms of gypsum). More than 80% sulfur in coal is organic sulfur, and the rest is mainly pyrite ($FeS_2$), gypsum ($CaSO_4$), and few ferric sulfates (Oliveira et al., 2011). Tuberculous-like, bulbous-like, nodular-like, and veined-like pyrites have been observed in coal. Sometime pyrite and gypsum assemblages are also found between coal bulks (Tang et al., 2018).

As mentioned in previous section, no matter coal combusts in the kiln or the precalciner, most of the $SO_2$ released from coal can be captured by CaO when the flue gas passes through the precalciner.

In raw materials, such as limestone, clay, and ferriferous material, nearly no organic sulfur is found, and inorganic sulfur in them mainly exists in the form of pyrite, gypsum, and ferric sulfates. These sulfur-containing minerals are generally symbiotic with calcite and quartz, therefore the sulfur characteristics of limestones, in terms of the content, species, morphology, and distribution, vary significantly depending on their geographical origins, especially for limestones from different parts of China (Xie et al., 2016). Furthermore, limestone contributes to approximately 85% wt. of raw meal, and only local limestones are used in cement production to reduce the transportation cost. Therefore, limestone is the dominant sulfur source, which contributes to nearly all $SO_2$ in the stack gas. However, few literatures focus on the sulfur characteristics of limestones used in cement plants. More importantly, their roles that they play in the sulfur cycles and then the $SO_2$ emission of stack gas remain largely unknown yet.

**1.4 The aim of the present study**

In the present study, limestones were collected from 80 NSP cement lines with $SO_2$ emission > 200 mg/Nm$^3$ (higher than the upper limitation of the national standard). Special attentions were paid on the sulfur content and species, morphology and distribution of pyrite in the limestones, and their influences on the $SO_2$ emission were analyzed, and then empirical relationships between $SO_2$ emission and the sulfur characteristics of limestones were established. The results will give a better understanding on the sulfur characteristics of limestones and their influences on the sulfur flow of the whole NSP cement line, the

relationships proposed can be used to predict the $SO_2$ emission based on the sulfur characteristics of limestones and to rationally utilize high-sulfur limestones in the cement industry.

## 2. The $SO_2$ emission of 80 NSP cement lines in China

Since numerous infrastructures are being built in central, eastern, and southern parts of China, more than 70% of cement plants are located in these densely populated regions. Eighty typical NSP cement lines, which didn't meet the $SO_2$ emission standard (upper limitation 200 mg/Nm$^3$ according to Chinese standard GB 4915-2013), were chosen for the case study, their location and production capacity are listed in Fig. 5.

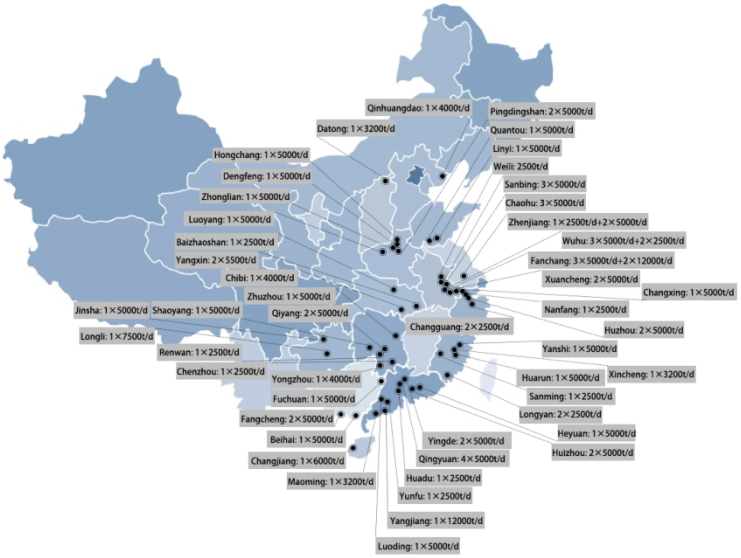


Fig. 5 The location and production capacity of 80 high-$SO_2$ emission NSP cement lines investigated

As we all know, limestone is one of main absorbents for desulfurization in various industries due to a slow reaction between $SO_2$ and $CaCO_3$. Since about 85% of raw meal is limestone, and limestone particles with fresh, reactive surface are contacted with flue gas sufficiently for 2-4 s at 80-120 ˚C and 10-20%RH during grounding, resulting in a significant reduction in $SO_2$ concentration when the flue gas

passes through the raw mill. For all NSP cement lines, the designed output capacity of the raw mill is slightly higher than the feed capacity of the NSP kiln system, therefore, the raw mill is usually turned off for 2-4 h per day for maintenance and repair. During this period, no flue gas goes through the raw mill, which means that no limestone is available for flue gas desulfurization. Therefore, a NSP cement line has, typically, two levels of $SO_2$ emissions, a low $SO_2$ emission when the raw mill is on, and a high $SO_2$ emission when the raw mill is off. These two levels of $SO_2$ concentrations of the stack gas were measured using a Tesco 350-pro flue gas analyzer with interval of 30 min for 48 h, and the average value was used as the $SO_2$ emission of the NSP cement lines when the raw mill was on or off. As shown in Fig. 6, the distribution of the $SO_2$ emission of the stack gas shifts left when raw mill is on, that is to say, the $SO_2$ concentration in the stack gas is much lower compared to that when raw mill is off, indicating that certain amount of $SO_2$ is captured by fresh limestone powder in the raw mill. When the raw mill is off, about 60% NSP cement lines have a $SO_2$ emission in the range of 500-1500 mg/Nm$^3$, while the most likely $SO_2$ emission range reduces to 300-1000 mg/Nm$^3$ when raw mill is on. For normal condition (raw mill on), the $SO_2$ emission of NSP cement lines can be classified into ultra-low ($SO_2 \leq 200$ mg/Nm$^3$), low (200 mg/Nm$^3$ < $SO_2 \leq 500$ mg/Nm$^3$), intermediate (500 mg/Nm$^3$ < $SO_2 \leq 1000$ mg/Nm$^3$), and high (> 1000 mg/Nm$^3$) emissions, accounting for 9%, 35%, 36%, and 20% of the NSP cement lines investigated, respectively.

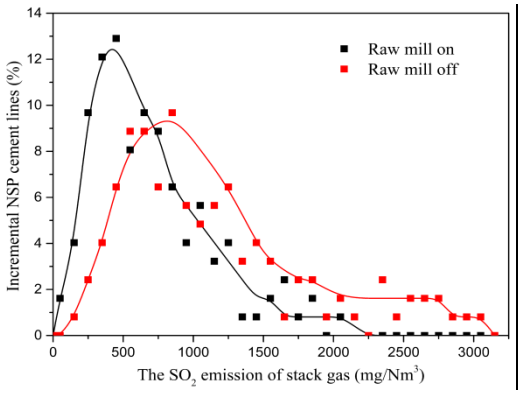


Fig. 6 The $SO_2$ emission distributions of 80 NSP cement lines investigated

## 3. The sulfur characteristics of their limestones

### 3.1 The sulfur content of limestones

To obtain representative samples, 100 kg of limestone was collected from each NSP cement plant and then ground into powder passing through an 80 μm sieve. About 100 g of limestone was sampled and then dried to constant weight. All sulfides and sulfates in limestone were dissolved and oxidized to sulfates (Vlisidis, 1966), the sulfur content was then measured indirectly by determining the amount of barium in the $BaSO_4$ precipitate (Chinese standard, GB/T 15057.8-1994).

Since sulfur in limestone mainly exists in the form of pyrite and gypsum, typical high-sulfur limestones, named by the initials of their origins, were selected to quantify the sulfide sulfur and sulfate sulfur. Sulfates were converted to barium sulfate by digesting the filtrate with an acidified $BaCl_2$ solution in an inert atmosphere to prevent oxidation of any sulfide sulfur, the sulfate sulfur was then measured by the determination of barium in the $BaSO_4$ precipitate (Chinese standard, GB/T 176-2008), and the sulfide sulfur was calculated by the difference between the total sulfur and the sulfate sulfur.

For the 80 NSP cement lines with high-$SO_2$ emission, the $SO_3$ content of their limestones is mainly in the range of 0.2-0.8% as shown in Fig. 7. Specifically, 46 limestones have a $SO_3$ content in the range

of 0.2-0.5%, and 23 limestones in the range of 0.6-0.8%, while 3 limestones have a $SO_3$ content higher than 1.0%. It can be inferred that only limestones with a $SO_3$ content higher than 0.2% result in a considerable $SO_2$ emission (>200 mg/Nm$^3$).

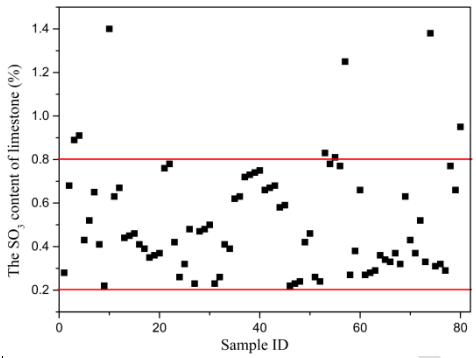


Fig. 7 The scatter distribution of the $SO_3$ content distributions of 80 limestones collected from high-$SO_2$ emission NSP cement lines

Typical limestones were selected to analyze the sulfur species and sulfur-containing minerals, the geographical origin or location was used as the ID of each limestone as shown in Table 2. Fig. 8 shows that sulfides are dominated in 7 out of 9 high-sulfur limestones, and less than 20% of sulfur in 5 limestones is contributed by sulfates, even no sulfate is detected in DT limestone. Only AH and DG limestones have a sulfate sulfur content higher than 50%, and nearly all sulfur in AH limestone is in the form of sulfates.

Table 2 The geographical origins or locations of typical high-sulfur limestones investigated

| Sample ID | Origin | Production Capacity |
|---|---|---|
| TP | Huizhou, Guangdong province | 2 × 5000 t/d |
| DT | Datong, Shanxi province | 1 × 3200 t/d |
| AH | Chaohu, Anhui province | 3 × 5000 t/d |
| CH | Chaohu, Anhui province | 3 × 5000 t/d |
| DG | Fanchang, Anhui province | 3 × 5000 t/d +2 × 12000 t/d |
| DF | Dengfeng, Henan province | 1 × 5000 t/d |
| HZ | Huzhou, Zhejiang province | 2 × 5000 t/d |
| ZC | Zhuzhou, Hunan province | 1 × 5000 t/d |

| | | |
|---|---|---|
| FJ | Longyan, Fujian province | 2 × 2500 t/d |
| HL | Yangjiang, Guangdong province | 1 × 12000 t/d |

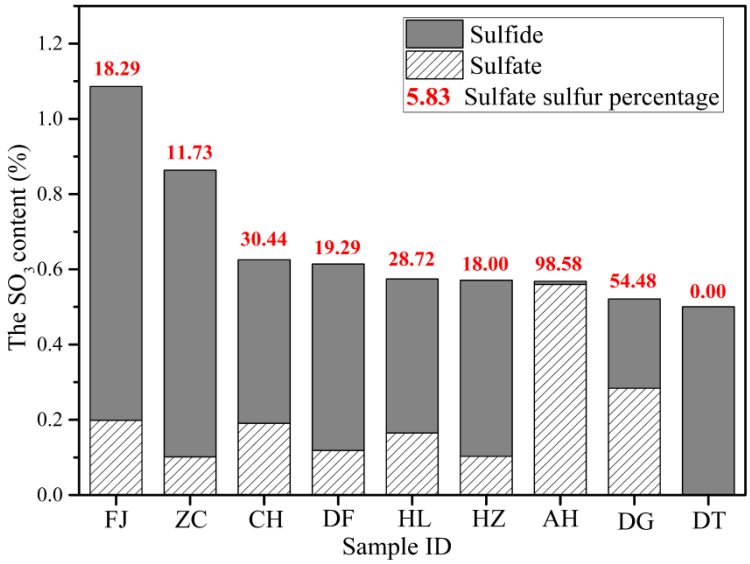


Fig. 8 The $SO_3$ content and the sulfate sulfur proportion of typical limestones (The limestone ID represents their geographical origins as listed in Table 2)

### 3.2 The sulfur species of limestones

The X-ray diffraction (XRD) analysis was used to characterize the crystalline phases in the limest ones. All tests was performed on a Bruker D8 advanced instrument equipped with a Cu anode X-ray tu be (40 kV, 250 mA) and an incident beam Ni monochromator (single Cu Ka1 line, λ = 1.5406 Å), using a step length of 0.02 ° and scan speed of 8 °/min. As shown in Fig. 9a, calcite, α-quartz, and dolomite ( $CaCO_3 \cdot MgCO_3$) are dominant minerals in all limestones, pyrite together with biotite ($K(Mg,Fe^{2+})_3(Al,Fe^{3+})Si_3O_{10}(OH,F)_2$), Pyrauxite ($Al_2[Si_4O_{10}](OH)_2$), illite ($K_{<1}(Al,R^{2+})_2[(Si,Al)Si_3O_{10}][OH]_2 \cdot nH_2O$, R is bivalent cations), anatase ($TiO_2$) are also identified in sulfides dominated limestones (e.g. DG, ZC, TP l imestones). Gypsum ($CaSO_4 \cdot 2H_2O$) as well as clinochlore ($Mg_5Al(Si_3Al)O_{10}(OH)_8$) and Jarosite ($KFe_3^{3+}[(OH)_6 \cdot SO_4]_2$) are found in sulfates dominated limestones (for instance, HZ, AH, HL). Therefore, sulf

ur in limestone mainly exists in the form of pyrite and sometime with minor gypsum, and these sulfur-c ontaining minerals prefer to coexist with biotite, dolomite, and clinochlore. For sulfides dominated lim estones, main diffraction peaks (2θ = 31.50°, 36.53°, 56.62° (Pourghahramani and Akhgar, 2015; Dong et al., 2005)) corresponding to pyrite are identified, and all the main diffraction peaks of pyrite shift to l ower diffraction angle compared with standard diffraction peaks, which can be attributed to its fluorine content (from 0.00% up to 5.76% as shown in Fig. 9b), as the S in the pyrite crystal can be replaced by F due to similar electronegativity and smaller ion radius (Dong et al., 2005). However, very low or near ly no diffraction peaks corresponding to pyrite are found in the HZ, AH, HL limestones with equal sulf ur content, indicating that sulfur in these limestones mainly exists in gypsum or pyrite with poor crystal linity (discussed in section 3.3 detailly).

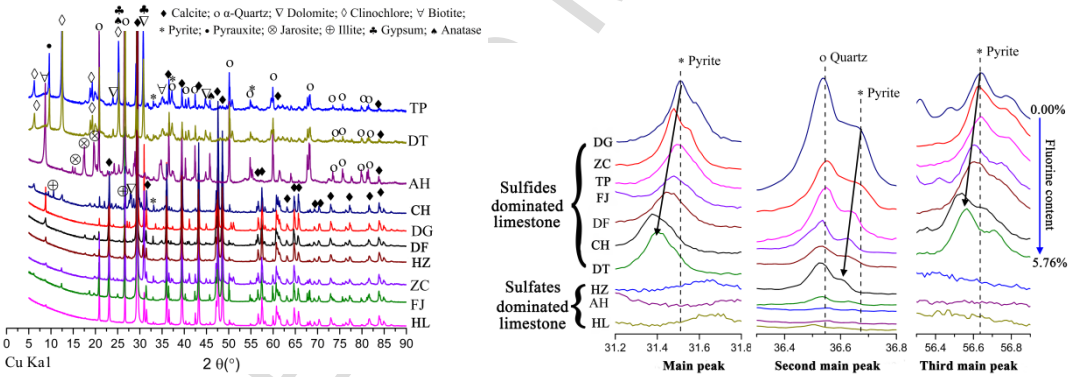


(a) The XRD patterns of high-sulfur limestones (b) Main diffraction peaks of pyrite in limestones

Fig. 9 XRD patterns of typical limestones collected from high-$SO_2$ emission NSP cement lines (The limestone ID represents their geographical origins as listed in Table 2)

### 3.3 The morphology and distribution of pyrite in limestones

Typical limestone particles were cross-sectioned and polished to observe the morphology and distribution of pyrite, and the sulfur content of the limestones was also tested and listed at the bottom of their optical microscope images. As shown in Fig. 10, the cross-sections of limestones present dark grey,

grey, yellow, and even brown. Notably, the sulfur contents of dark grey and grey limestones are relatively higher than those of light yellow and brown limestones. Layered and disseminated bulk pyrites (light with metallic luster spot) together with impurities are observed in dark grey and grey limestones (normally metamorphic or sedimentary rocks formed in reducing atmosphere). In contrast, nearly no bulk pyrite is found in light yellow and brown limestones, which are generally calcite sedimentary rocks containing trivalent iron oxides or hydroxides. It is well known, pyrite only exists in reducing atmospheres, however trivalent iron oxides or hydroxides are formed in oxidizing atmospheres. Therefore, pyrite is usually observed in dark grey and grey limestones, whereas light yellow and brown limestones have no bulk pyrite and much lower sulfur content.

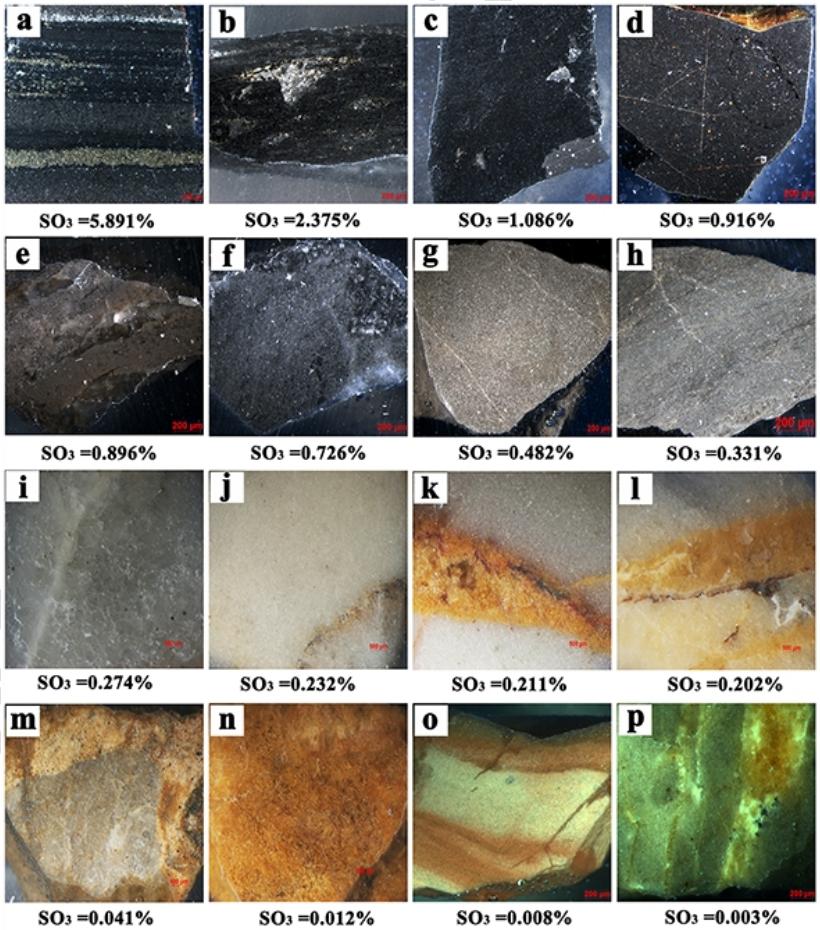


Fig. 10 Optical microscope images of limestones with different sulfur contents

Polarized light microscope (ZEISS Stemi 2000) was also employed to observe the morphology of the pyrites in limestones. Light zones with metallic luster are bulk pyrites as shown in Fig. 11, and the rest grey or dark grey zones are mainly calcite with mineral impurities, such as quartz, biotite, dolomite. According to the morphology and distribution, bulk pyrites in limestone can be classified into four categories: euhedral pyrite, framboidal pyrite, disseminated pyrite, and metasomatic pyrite. Rectangle or polygon pyrites (theoretically cubic or octahedron as shown in Table 3) with size of 50-200 μm are observed in euhedral pyrite limestone (Fig. 11 a-d), whereas pyrite framboids (actually pyritohedron) with size of 500 nm - 2 μm assemble to form polyframboid (5-20 μm) and then even pyrite layer in framboidal pyrite limestone (Fig. 11 e-h). These two pyrites are highly or fully crystallized and usually presented in sedimentary rocks, especially for basic and ultrabasic rocks. Furthermore, pyrite framboids have a relatively lower S/Fe molar ratio (such as $Fe_3S_4$), thus framboidal pyrites tend to accumulate and form euhedral pyrites when sufficient sulfur is available (Sawlowicz, 1993). Pyrites with various shape are disseminated in limestone densely as shown in Fig. 11 i-l, quartz (dark grey) together with calcite are intergrown inside and outside of bulk pyrites. Minerals with parallel texture (lines spacing of 5-10 μm) are found in Fig. 11 m-p, and metasomatic pyrites with irregular shape coexist in the interlayer of parallel-textured minerals.

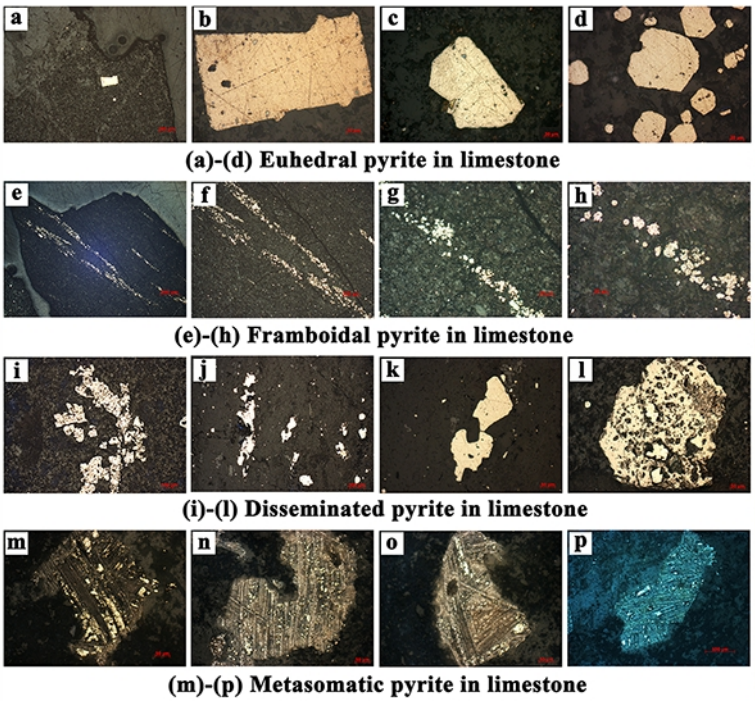


Fig. 11 The morphology and distribution of bulk pyrites in Polarized light microscope images

Limestone particles were immersed in epoxy resin and then polished carefully by machine to eliminate personal errors. The morphology and distribution of pyrites were characterized by a scanning electron microscope (ZEISS, EVO 50) under backscattered electron imaging (BEI) mode (accelerating voltage of 20 kV, certified standards were used for calibration). As shown in Fig. 12, euhedral pyrites have regular shape, framboidal pyrites contain multi-scale framboids with different size, both of them assemble to form pyrite layer in high-sulfur limestones. Disseminated and metasomatic pyrites are also seen in BEI images, their geometrical morphology, crystallinity, and size are summarized in Table 3. Mapping and point modes of energy dispersive spectrometer (EDS, Oxford INCA X-Max) were used to obtain the element composition, then pyrites together with associated minerals were discussed by comparing the elements distribution and the element molar ratio of interest zones.

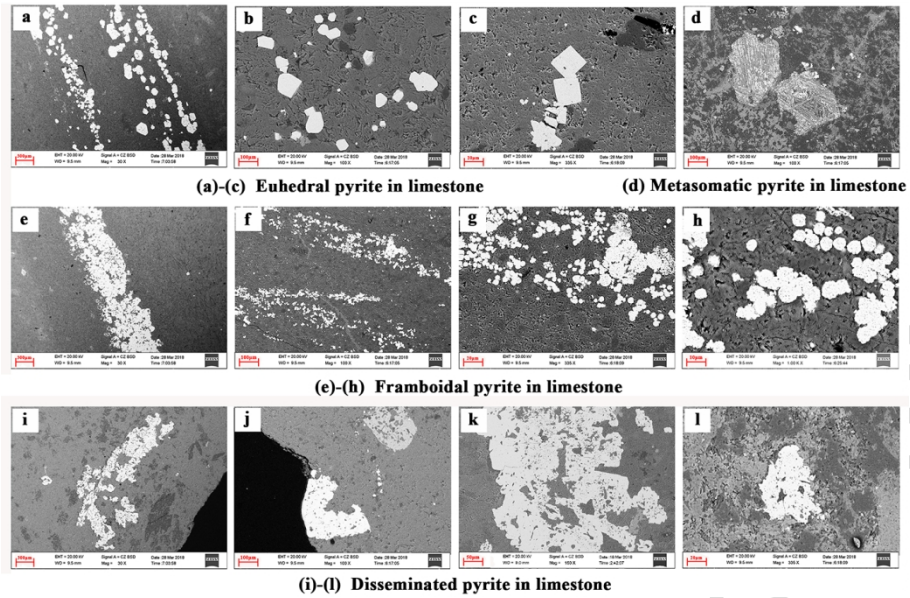


Fig. 12 The morphology and distribution of pyrites in the BEI images

Table 3 The theoretical morphology of pyrites in limestones

| Distribution | Theoretical geometry | Theoretical morphology | Theoretical shape | Crystallinity | Size (μm) | Reference |
|---|---|---|---|---|---|---|
| Euhedral pyrite | Cubic or Octahedron | 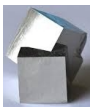 | 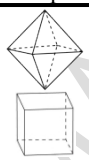 | Well crystallized | 50-200 | (Ostwald and England, 1979) |
| Framboidal pyrite | Polyframboid or Pyritohedron |  |  | Highly crystallized | 10-50 | (Sawlowicz, 1993) |
| Disseminated pyrite | Disseminated texture | 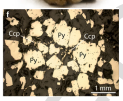 | Irregular shape | Poor crystallized | 10-100 | (Höhn et al., 2017) |
| Metasomatic pyrite | Metasomatic or layered texture |  | Irregular shape | Poor crystallized | 2-20 | (Kouhestani et al., 2017, Xiao et al., 2016) |

### 3.3.1 The euhedral pyrite in limestone

The euhedral pyrites (light zones) usually have well crystallinity as a cubic or octahedron as shown in Fig. 13, only Fe and S are identified by EDS mapping analysis in light zone, with S to Fe molar ratio of 2.08 according to the element composition of point A (Table 4), indicating nearly no impurity is existed in the pyrite. In addition, the distributions of Si, Al, Mg, and Fe are highly overlapped, and the round-like or belt-like dark grey zones are mainly biotite with quartz according to the element composition of point B. Both pyrite and biotite are surrounded by nearly pure calcite, as only 0.23% Mg

is measured at point C, indicating that minor dolomite is coexisted with calcite (grey zone) in the limestone (DG limestone in Fig. 9).

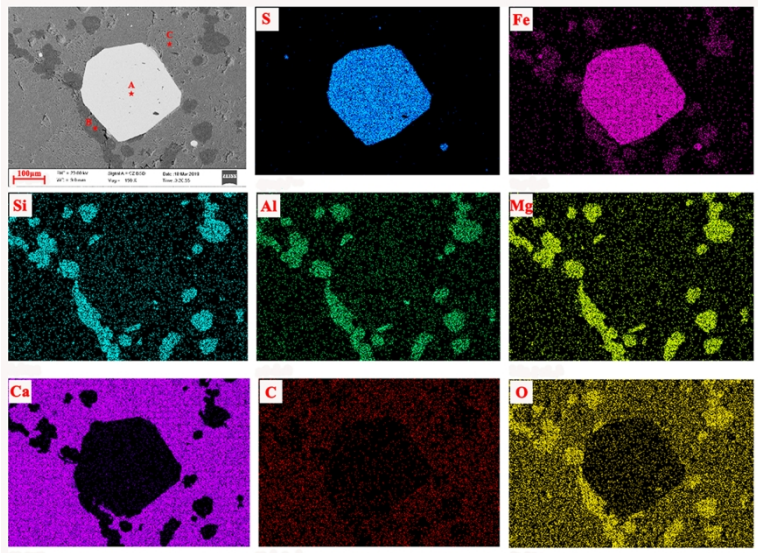


Fig. 13 SEM image and element distributions of limestone with euhedral pyrite

Table 4 Element composition of interest points in Fig. 13 determined by EDS

| Element | Atomic percent | | |
|---|---|---|---|
| | Point A | Point B | Point C |
| O | — | 66.78 | 72.54 |
| S | 67.59 | — | — |
| Fe | 32.41 | 3.88 | — |
| Ca | — | 0.10 | 27.23 |
| Si | — | 10.32 | — |
| Al | — | 6.89 | — |
| Mg | — | 12.03 | 0.23 |
| Total | 100.00 | 100.00 | 100.00 |

Note: — undetected.

### 3.3.2 The framboidal pyrite in limestone

Zone A in Fig. 14 is mainly pyrite with a small amount of fluoride, as the S to Fe molar ratio is 2.08 and the F content is 4.75% according to the element composition of zone A (Table 5). While zone B has a higher concentration of Si, Al, Mg, Ca, K, and the molar ratio of these elements is close to that of biotite ($K(Mg,Fe^{2+})_3(Al,Fe^{3+})Si_3O_{10}(OH,F)_2$), which is usually found in basic and ultrabasic rocks. Thus, the mineral composition of zone B is calcite with biotite, which can be firmly proved by its XRD pattern (CH in Fig. 9). As shown in the BEI image, multi-framboids (5.0 - 20.0 μm) with several framboidal or

fine-grained microspheres (0.5-3.0 μm) are grouped together to form spherical or sub-spherical shaped clusters. EDS mapping analysis confirms that the pyrite clusters with abundant F are surrounded by calcite and biotite, as abundant of Si, Al, Mg, Ca, and K are found in grey zone.

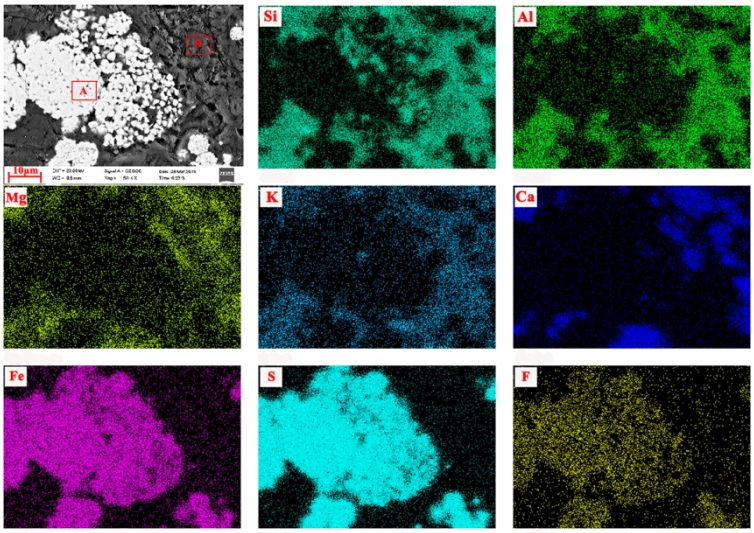


Fig. 14 SEM image and element distributions of limestone with framboidal pyrite

Table 5 Element composition of interest zones in Fig. 14 determined by EDS

| Element | Atomic percent | |
|---|---|---|
| | Zone A | Zone B |
| O | 7.08 | 67.80 |
| S | 59.27 | — |
| Fe | 28.45 | 0.96 |
| Ca | — | 4.50 |
| Si | 0.45 | 12.63 |
| Al | — | 6.00 |
| Mg | — | 4.39 |
| F | 4.75 | 1.53 |
| K | — | 2.19 |
| Total | 100.00 | 100.00 |

Note: — undetected.

### 3.3.3 The disseminated pyrite in limestone

As shown in Fig. 15, the irregular light zones are connected with each other and disseminated in the limestone. EDS mapping analysis presents that S, Fe, and F are concentrated in light zone, indicating that light zone is disseminated pyrite with abundant F. Dark grey zone is rich in Si, Mg, and Al, and the O concentration is relatively higher than other zones, therefore dark grey zone is mainly quartz with seraphinite. Comparatively, grey zones have a high concentration of Ca and O as well as low

concentration of Si, Mg, and Al, thus it can be inferred that grey zone is mainly calcite with small amount of seraphinite. Element composition of interest points listed in Table 6 confirms that the mineral composition of point A in light zone is pyrite with fluoride, as the content of F is as high as 5.76%. Since F has a smaller atomic radius than S, a small proportion of S in pyrite crystal is replaced by F to form $FeF_2$ (DT limestone in Fig. 9). Point B in the grey zone is calcite with quartz, whereas point D is nearly pure calcite with minor dolomite and pyrite. For point C in dark grey zone, quartz is the dominant mineral, with few seraphinite and calcite.

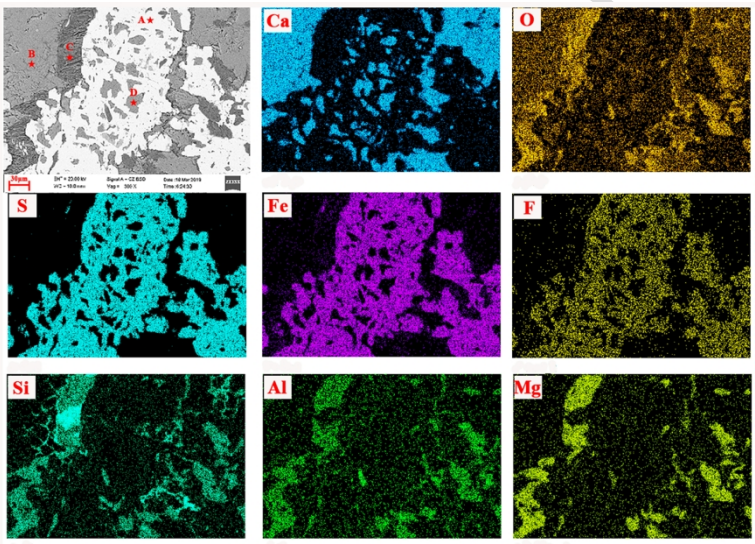


Fig. 15 SEM image and element distributions of limestone with disseminated pyrite

Table 6 Element composition of interest points in Fig. 15 determined by EDS

| Element | Atomic percent | | | |
|---|---|---|---|---|
| | Point A | Point B | Point C | Point D |
| O | — | 72.67 | 63.06 | 72.78 |
| S | 63.49 | — | — | 0.17 |
| Fe | 29.96 | — | 0.18 | 0.34 |
| Ca | — | 11.35 | 0.12 | 26.52 |
| Si | 0.51 | 15.98 | 35.65 | — |
| Al | 0.28 | — | 0.38 | — |
| Mg | — | — | 0.61 | 0.19 |
| F | 5.76 | — | — | — |
| Total | 100.00 | 100.00 | 100.00 | 100.00 |

Note: — undetected.

### 3.3.4 The metasomatic pyrite in limestone

Fig. 16 indicates dark grey zones have very high concentration of Si according to EDS mapping analysis (point B in Table 7), thus dark grey zones are mainly consisted of quartz with few biotite. Grey zones are dominated by calcite with quartz due to higher Ca concentration, and pyrites (light spots) are only distributed in a textured zone. More important, the textured zone contains very high concentration of Ti, Fe, Al, and S, the fibrous or layered minerals are mainly octahedrite ($TiO_2$) and ilmenite ($Fe_2O_3 \cdot 3TiO_2$) isomorph with Mg (point C). Either metasomatic pyrite (point A in light zones) or mixture of dolomite, Jarosite, pyrophyllite, illite, and biotite are coexisted in the interlayer of octahedrite and ilmenite, all these minerals have been identified by XRD patterns (TP limestone in Fig. 9). Additionally, Ti, Fe, Al, and even K have similar distribution patterns in limestone, whereas S is only concentrated in the zone with high amount of Fe, indicating pyrite prefer to coexisted with ilmenite and octahedrite.

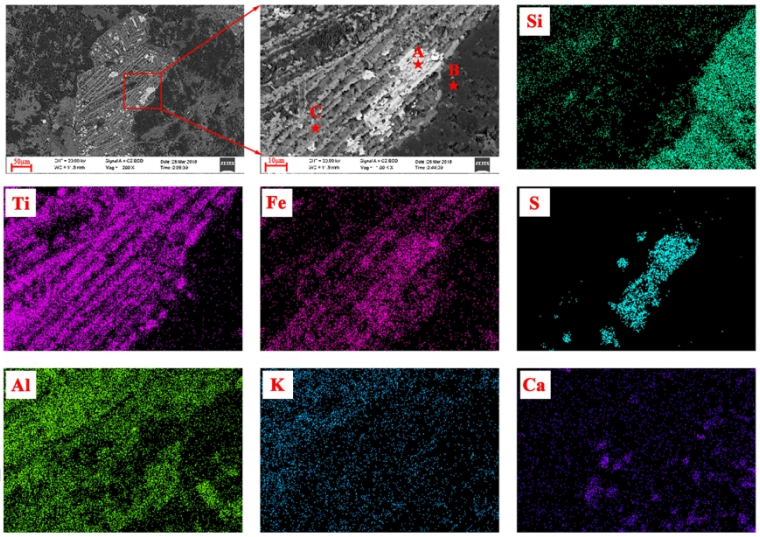


Fig. 16 SEM image and element distributions of limestone with metasomatic pyrite

Table 7 Element composition of interest points in Fig. 16 determined by EDS

| Element | Atomic percent | | |
|---|---|---|---|
| | Point A | Point B | Point C |
| O | 28.07 | 67.36 | 70.29 |
| S | 40.70 | — | 0.24 |
| Fe | 19.24 | 0.45 | 5.18 |
| Ca | — | 0.74 | 0.42 |

| | | | |
|---|---|---|---|
| Si | 1.85 | 30.48 | 6.78 |
| Al | 1.27 | 0.47 | 5.91 |
| Mg | — | 0.33 | 1.82 |
| K | 0.23 | 0.09 | 0.38 |
| Ti | 8.64 | 0.08 | 8.98 |
| Total | 100.00 | 100.00 | 100.00 |

Note: — undetected.

### 3.4 Thermal decomposition process of 4 typical limestones

Since significant differences in pyrite morphology and accompanying elements are observed in limestones, thermogravimetric (TG) analysis (NETZSCH TG 209 F1 Libra) was carried out on four typical limestones (a low impurity limestone (HZ, a low-sulfur limestone as a reference), a euhedral pyrite limestone (DG, a high-sulfur limestone), a framboidal pyrite limestone (CH, a high-aluminum and silicon limestone), and a disseminated pyrite limestone (DT, a high-fluorine limestone)), to clarify the decomposition process of pyrite in limestones. The TG test was conducted in nitrogen atmosphere with a gas flow rate of 100 mL/min, equilibration at 40°C for 10 min, and a heating rate of 10 °C/min up to 1350°C.

Differential thermogravimetric (DTG) curves as shown in Fig. 17 have three valleys in the range of 450-600 ˚C, 600-880 ˚C, 1100-1300 ˚C, corresponding to decomposition of sulfides (mainly pyrite), carbonates (calcite with minor dolomite), and sulfates (gypsum), respectively (Hansen et al., 2003). Then the weight losses in these three temperature ranges are calculated according to TG curves and listed in Table 8. HZ limestone has nearly on pyrite and gypsum as their weight losses are as low as 0.68% and 0.17%, respectively, and the weight loss due to decomposition of calcite reaches 40.59%, indicating that HZ limestone has a calcite content of 92.3%. In contrast, DG limestone has two obvious valleys due to

the decomposition of pyrite and gypsum, and their weight losses are as high as 2.71% and 1.31%, respectively. Since the weight loss in the range of 600-880 ˚C is only 28.46%, CH limestone is a low-calcium limestone (calcite content of 64.68%) due to aluminum and silicon impurities. Additionally, the decomposition temperature of calcite in CH limestone is 835 ˚C, and reduces to 785 ˚C for DT limestone, suggesting that the calcite in DT limestone has a lower decomposition temperature. The phenomenon can be attributed to its F content (5.76%), as $CaF_2$ is a typical mineralizer to decrease the decarbonation and clinkerlization temperatures and to accelerate the solid-state reaction (Hansen et al., 2003, Johansen and Christensen, 1979).

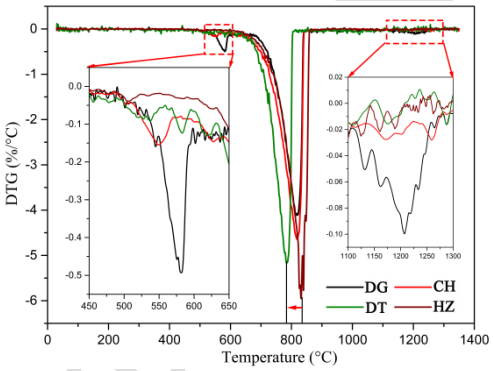


Fig. 17 The DTG curves of limestones collected from high-$SO_2$ emission NSP cement lines (The limestone ID represents their geographical origins as listed in Table 2)

Table 8 Weight losses of 4 typical limestones in different temperature ranges calculated from TG curves (The limestone ID represents their geographical origins as listed in Table 2)

| Temperature rang (˚C) | | 0-400 | 400-650 (I) | 650-880 (II) | 880-1100 | 1100-1300 (III) |
|---|---|---|---|---|---|---|
| Reaction | | Chemically bound water loss | Sulfides decomposition | Carbonates decomposition | — | Sulfates decomposition |
| Mineral | | — | Pyrite | Calcite with minor dolomite | — | Gypsum |
| Limestone ID | DG | 0.22 | 2.71 | 28.46 | 0.76 | 1.31 |
| | CH | 0.11 | 1.71 | 35.35 | 0.24 | 0.53 |
| | DT | 0.39 | 1.67 | 32.22 | 0.92 | 0.09 |
| | HZ | 0.05 | 0.68 | 40.59 | 0.19 | 0.17 |

**4. Relationships between the $SO_2$ emission of stack gas and the sulfur characteristics of limestones**

From the analysis above, it can be concluded that the sulfur content and species as well as the distribution and morphology of pyrites in limestones are key factors influencing the $SO_2$ emission of NSP cement lines, although fuel, other raw materials, and air feed, the capacity and operation conditions of NSP cement lines also influence on the $SO_2$ emissions of the stack gas. The $SO_2$ emission of 80 NSP cement lines (>200 mg/Nm$^3$) is correlated to the sulfur characteristics of limestones to clarify their roles.

**4.1 Relationship between $SO_2$ emission and the sulfur content of limestones**

Compare with raw mill off, raw mill on leads to a $SO_2$ reduction of 200-1000 mg/Nm$^3$ depending on the $SO_3$ content of limestone as shown in Fig. 18. For the 67 cement lines of all 80 cement lines investigated, these two $SO_2$ emissions increase linearly with the $SO_3$ content of their limestones. Some NSP lines (triangle points) have much lower $SO_2$ emission no matter if the raw mill is on or off, as the certain proportion of sulfur in the limestone exists in form of sulfates (mainly gypsum). The $SO_3$ content of limestone corresponding to ultra-low ($SO_2 \leq 200$ mg/Nm$^3$), low (200 mg/Nm$^3$ <$SO_2 \leq 500$ mg/Nm$^3$), intermediate (500 mg/Nm$^3$ < $SO_2 \leq 1000$ mg/Nm$^3$), and high (> 1000 mg/Nm$^3$) $SO_2$ emissions are < 0.2%, 0.2-0.4%, 0.4-0.7%, and > 0.7%, respectively. Thus, the $SO_2$ emission of a given NSP cement line can be roughly estimated based on the $SO_3$ content of limestone used.

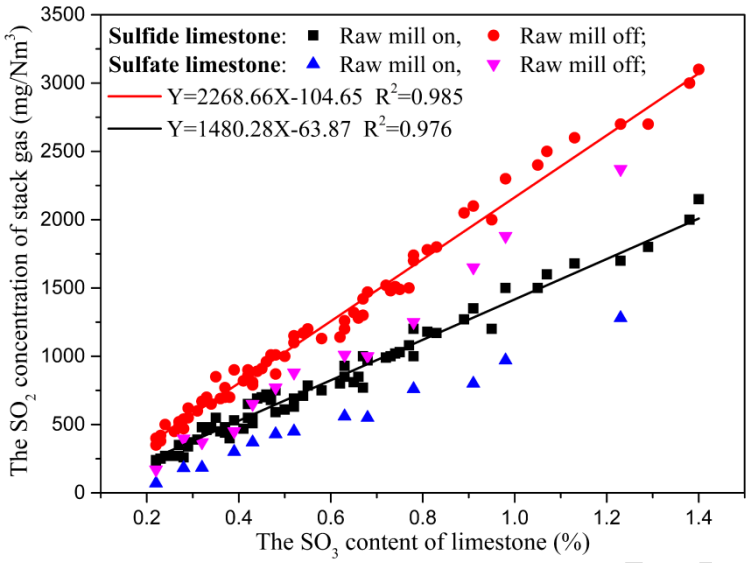


Fig. 18 Relationship between the $SO_2$ emission of stack gas and the $SO_3$ content of limestones

### 4.2 Relationship between $SO_2$ emission and sulfate sulfur in limestones

Influences of the sulfate sulfur on the $SO_2$ emission is discussed by comparing the $SO_2$ emission of 7 NSP cement lines, in which limestones with equal $SO_3$ content (0.55 ± 0.03%) are used. The $SO_2$ emission reduces gradually with the increase of sulfide sulfur proportion as shown in Fig. 19. For instance, when the sulfur in the limestone is pure pyrite, the $SO_2$ emissions are 650 mg/Nm$^3$ and 900 mg/Nm$^3$, respectively, for raw mill on and off. Whereas the corresponding $SO_2$ emission are only 300 mg/Nm$^3$ and 450 mg/Nm$^3$, when the sulfate sulfur proportion of limestone is 98.6%. That is to say, about 50% of $SO_2$ is reduced, as 40-80% of sulfates can be solidified into clinker, while all sulfides are decomposed and release $SO_2$ in 400-600 ˚C during preheating (Hu, 2007). In addition, when the sulfate sulfur proportion of limestone increased from 0% to nearly 100%, the difference in $SO_2$ emission between the raw mill being on and off is decreased from 250 mg/Nm$^3$ to 150 mg/Nm$^3$, indicating that the desulfurization capacity of the raw mill is more pronounced when pyrite dominated limestone is used. The reason lays in that sulfides mainly decompose in C2/C3 cyclones of the preheater and then the

released $SO_2$ only passes through the raw mill before discharging into the atmosphere, in contrast, the sulfates decompose in the kiln and the released $SO_2$ can be captured by CaO generated in the precalciner and then by $CaCO_3$ in the raw mill.

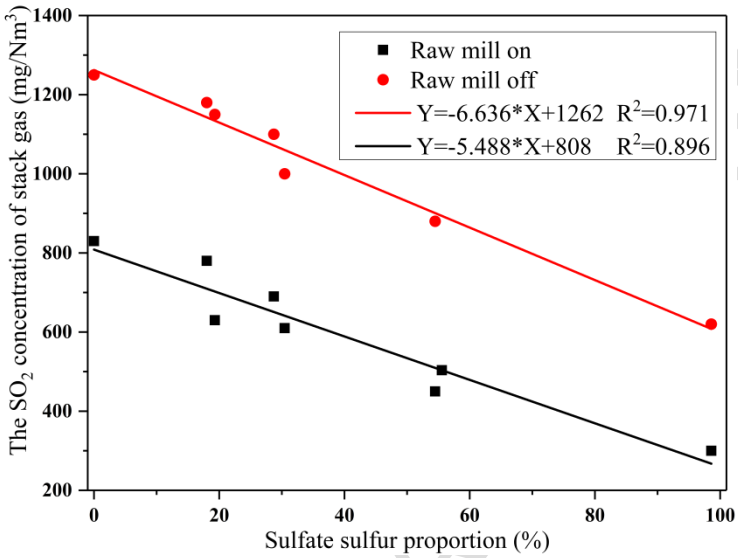


Fig. 19 Relationship between the $SO_2$ emission of stack gas and the sulfate sulfur proportion of limestones

### 4.3 Relationship between $SO_2$ emission and the morphology of pyrite in limestones

By comparing the $SO_2$ emission of 15 NSP cement lines with the average emission obtained from section 4.1, influences of the morphology and distribution of pyrites in limestones are clarified. As shown in Fig. 20, euhedral pyrite limestone leads to a slightly higher $SO_2$ emission than the average emission, framboidal and disseminated pyrite limestones have a $SO_2$ emission nearly equaled to the average emission, whereas metasomatic pyrite limestones results in a lower $SO_2$ emission compared with the average emission. For example, when limestones with $SO_3$ content of 0.68% are used, metasomatic pyrite limestone leads to $SO_2$ emissions of 550 mg/Nm$^3$ (raw mill on) and 1000 mg/Nm$^3$ (raw mill off), which are, respectively, 540 mg/Nm$^3$ and 620 mg/Nm$^3$ lower than the corresponding $SO_2$ emissions of euhedral

pyrite limestone. Therefore, the morphology and distribution of pyrites in limestones also has a significant influence on the $SO_2$ emission of NSP cement lines.

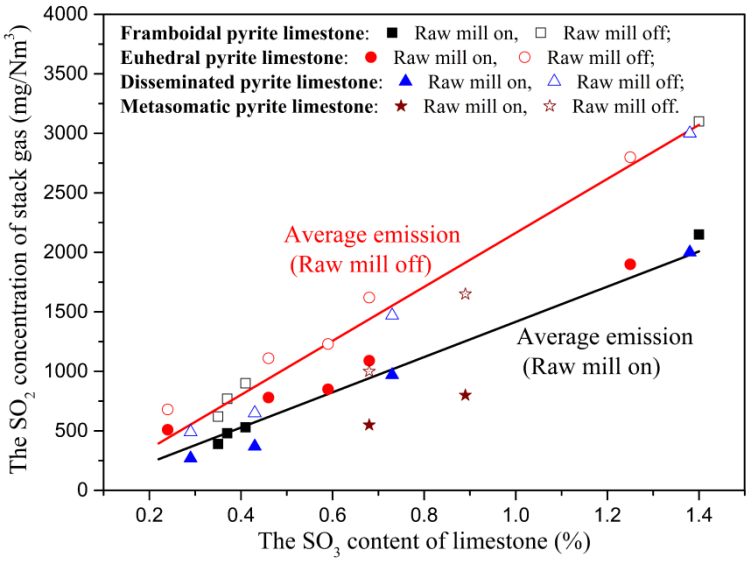


Fig. 20 Relationship between the $SO_2$ emission of stack gas and the morphology of pyrite in limestones

## 5. The mechanism of sulfur characteristics influencing the $SO_2$ emission of NSP cement lines

Based on the experiment data, sulfur flow in a typical NSP cement line was summarized as shown in Fig. 21, then influences of the sulfur characteristics on the $SO_2$ emission were discussed. For NSP cement lines with the same operating conditions, there is no doubt that a lower sulfur content of limestone leads to a lower $SO_2$ emission. Furthermore, sulfides in limestone decompose in the preheater (Equation ① in Fig. 21), then only small proportion of $SO_2$ released can be captured by $CaCO_3$ whilst passing through the upper cyclones and raw mill before exhausting (Equation ⑤). In contrast, sulfates (mainly gypsum) in limestone decompose and release $SO_2$ in the kiln (Equation ②), meanwhile the released $SO_2$ can be captured by alkali and CaO in the kiln and precalciner (Equation ③ and ④), and $CaCO_3$ also has a minor desulfurization capacity (Equation ⑤) whilst passing through the preheater and the raw mill.

Therefore, sulfates dominated limestone has a much lower $SO_2$ emission compared to sulfides dominated limestone with equal sulfur content.

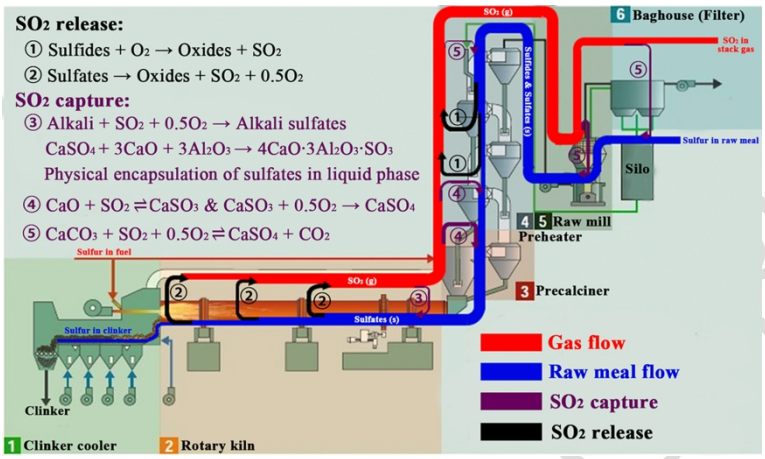


Fig. 21 Schematic sulfur flow, $SO_2$ release and capture in a typical NSP cement line

The morphology of pyrites in limestone also has dramatic influences on the $SO_2$ emission of NSP cement lines. The Mohs hardness of a fully crystallized pyrite is 6.5, while that of calcite is only 3.0 (Wells et al., 2005). Therefore, large-sized euhedral pyrites are easily stripped off the mother limestone during grinding and then crushed into smaller particles (as shown in Fig. 22a), leading to rapid oxidation of pyrite and release of $SO_2$. Thus, the $SO_2$ emission due to decomposition of euhedral pyrite is slightly higher than the average $SO_2$ emission. Framboidal pyrite also has good crystallinity, and consequently pyrite usually appears on the surface of limestone particles after being crushed and ground (Fig. 22b). On another hand, Framboidal pyrite limestone usually contains abundant K and F, $K_2SO_4$ is a stable mineral which never decomposes during clinkerization (Choi and Glasser, 1988), and fluoride is a typical mineralizer to reduce clinkerization temperature and to increase the amount of the liquid phase (calcium aluminate ($C_3A$) and calcium aluminoferrite ($C_4AF$)), all of which are helpful to solidify more sulfur into

clinker (Equation ③). Therefore, framboidal pyrite limestone results in a slightly lower $SO_2$ emission compared to euhedral pyrite limestone.

During crashing and grinding processes of limestone, cracks will not be prolonged at the boundary between calcite and pyrite with poor crystallinity and irregular shape. Since disseminated pyrites are coexisted with quartz, seraphinite, biotite, and calcite, a higher proportion of disseminated pyrite is covered by associated minerals during grinding (Fig. 22c), which leads to delayed $SO_2$ release and a longer route and time to exhaust. Finally, a higher proportion of $SO_2$ can be captured by $CaCO_3$ or even CaO during discharging. In addition, higher amounts of Al, F are found in disseminated pyrite limestone, then more $C_3A$ and $C_4AF$, the main sulfur-encapsulating minerals, are generated during clinkerization (Chen, 2013; Li et al., 2014). As a result, disseminated pyrite limestone leads to a lower $SO_2$ emission than framboidal pyrite limestone. Metasomatic pyrite generally coexists with octahedrite, ilmenite, pyrophyllite, Jarosite, dolomite, and biotite, thus pyrite is also covered by these minerals during grinding (Fig. 22d). More importantly, $TiO_2$ is a typical catalyzer to accelerate the oxidation reaction of $SO_2$ to $SO_3$ (Wang et al., 2015; Ma et al., 2008; Lapina et al., 1999; Kamata et al., 2001), and $SO_3$ is much more reactive and easily captured in the NSP cement line compared to $SO_2$, as the reaction rate of route 1 is much faster than that of route 2 (Burdett et al., 1979; Shih et al., 2004). Additionally, high Al, Fe and Mg contents are also helpful to solidify more sulfur into clinker. Thus, metasomatic pyrite limestone has a much lower $SO_2$ emission compared to other pyrite limestones.

Route 1: $SO_2 + \frac{1}{2}O_2 \rightleftharpoons SO_3$ & $\mathrm{CaO} + \mathrm{SO_3} \rightarrow CaSO_4$

Route 2: $\mathrm{CaO} + \mathrm{SO_2} \rightleftharpoons CaSO_3$ & $CaSO_3 + \frac{1}{2}O_2 \rightarrow CaSO_4$

In summary, the $SO_2$ emissions of a NSP cement line is mainly related to the sulfur content and species of limestone used, as the sulfides and sulfates in limestone are, respectively, decomposed in the preheater and the kiln, resulting in different $SO_2$ capture opportunities. However, the morphology and distribution of pyrite in limestones also have a significant influence on the $SO_2$ concentration of stack gas. The reasons can be attributed to that bulk pyrites with larger size and good crystallinity are easily stripped off the limestone and then ground into fine particles, therefore $SO_2$ is rapidly released due to the direct exposure to the flow gas. Associated minerals with pyrite (accompanying elements, especially for Ti, F, K, and Al) can reduce the clinkerization temperature, increase the amount of liquid phase, and accelerate the desulfurization reaction by oxidizing $SO_2$ to $SO_3$, all of which are benefit to solidify and encapsulate more sulfur into clinker.

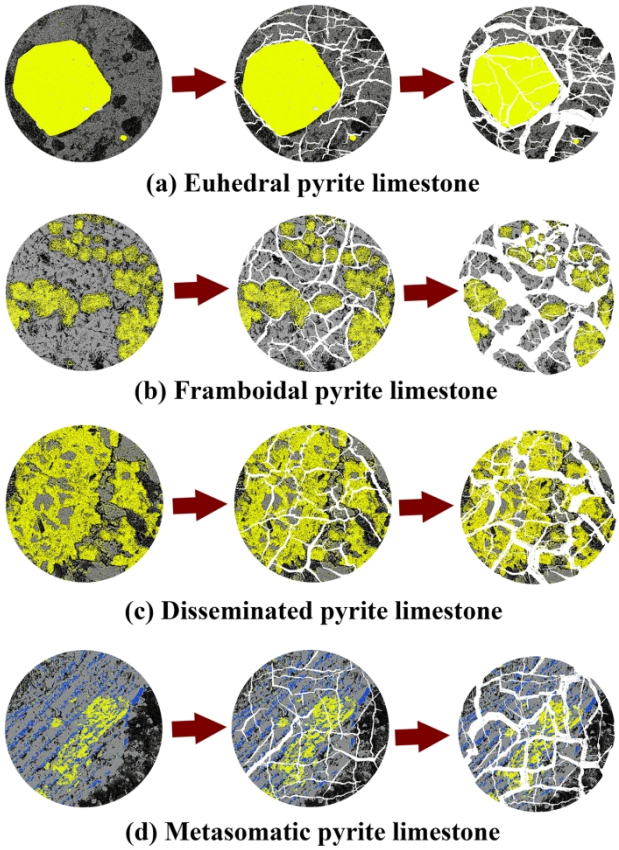


Fig. 22 Schematic diagram of crashing and grinding processes of limestones with different pyrites

## 6. Conclusions and prospect

Since $SO_2$ released from fuel can be captured by CaO in the precalciner, limestone is the dominant sulfur source, which contributes to nearly all $SO_2$ in the stack gas. Due to limited availability of low-sulfur limestone, high-sulfur limestone has therefore been more and more utilized in cement industry, leading to higher $SO_2$ emission and finally to either acid rain or smog. However, the sulfur characteristics of limestones used in cement plants remained largely unknown yet, and their influences on the sulfur cycles and $SO_2$ emission were investigated mainly on laboratory experiments in available literatures, which are quite different from the cement industry.

The sulfur in limestone mainly existed in the form of pyrite, and sometime gypsum is also found. Euhedral pyrite, framboidal pyrite, disseminated pyrite, and metasomatic pyrite are observed in limestones, quartz, biotite, and seraphinite are usually coexisted with bulk pyrites. F is identified in framboidal and disseminated pyrites, whereas metasomatic pyrite as well as dolomite, diaspore and biotite are coexisted in the interlayer of octahedrite and ilmenite. Based on the data collected from 80 full-scale NSP cement lines, the $SO_2$ emissions no matter if the raw mill is on or off increase linearly with the $SO_3$ content of limestone, and sulfates lead to a 50% reduction in $SO_2$ emission compared to sulfides. Compared with the average $SO_2$ emission, euhedral pyrite leads to a slightly higher $SO_2$ emission, whereas metasomatic pyrites result in a much lower $SO_2$ emission, which can be attributed to the effects of accompanying elements (Ti, F, K, and Al et al.) on the desulfurization reaction and clinkerization in the NSP cement line.

The sulfur flow, $SO_2$ release and capture in a NSP cement line were established based industrial data and literature review, which can be used to predict the $SO_2$ emission based on the sulfur characteristics of limestone and to rationally utilize high-sulfur limestone in cement industry. However, $SO_2$ released from other raw materials or alternative fuels was not taken into consideration in the present study. For instance, local available high-sulfur solid wastes as ferriferous or siliceous materials and coprocessing high-sulfur organic wastes in NSP cement kiln may also lead to high $SO_2$ emission, particularly for municipal solid wastes, waste tire and etc. Therefore, the sulfur characteristics, pretreatment, feeding

points (or locations) and methods of sulfur-containing wastes on the $SO_2$ emission should be extensively investigated in the future.

**Acknowledgments**

This work was funded by the National Natural Science Foundation of China (No. 51872096), the Guangdong Science and Technology Program (2016A020221009), the Guangdong Special Support for Youth Science and Technology Innovation Talents (2015TQ01C312), and the Pearl River Science and Technology Nova Program of Guangzhou (201610010098). Their financial supports are gratefully acknowledged.

**Conflict of interest**

The authors declare that they have no conflict of interest.

**References**

Ávila, I., Milioli, F.E., Crnkovic, P.M., 2005. kinetics study on the sorption of $SO_2$ by limestone through thermogravimetry. 18th International Congress of Mechanical Engineering, Ouro Preto, Brazil.

Burdett. N.A., Hotchkiss. R.C., Fieldes. R.B., 1979. $SO_3$ formation and retention in coal-fired fluidized bed combustors. AIChE 57, 1–11.

China5e, 2014. China's environmental pollution status: Far more terrible than the smog. http://www.china5e.com/news/news-872297-1.html,-06-10. (In Chinese)

China gateway to corrosion and protection, 2011. Corrosion related to acid rain. http://www.ecorr.org/journal/wangzhanhuikan/2011nian06yuedierqi/2013/0606/5678.html. (In Chinese)

Chinese Standard. GB 4915-2013. Emission standard of air pollutants for cement industry.

Chinese standard. GB/T 15057.8-1994. Testing method for determination of sulfur in limestone: Barium sulfate gravimetric method and combustion-potassium iodate titration method.

Chinese standard. GB/T 176-2008, Testing method for cement: Chemical analysis of cement.

Chen, X., 2013. Barium sulphoaluminate (strontium) calcium cement. Science Press, Beijing.

Chen, X., Mulder, J., 2007. Atmospheric deposition of nitrogen at five subtropical forested sites in South China. Sci. Total Environ. 378, 317–330.

Choi, G.S., Glasser, F.P., 1988. The sulphur cycle in cement kilns: Vapour pressures and solid phase stability of the sulphate phases. Cem. Concr. Res. 18, 367–374.

Dong, Y., Zheng, Y., Duan, H., Sun, Y., Chen, Y., 2005. Formation of pyrite ($FeS_2$) thin nano-films by thermal-sulfurating electrodeposition films at different temperature. Mater. Lett. 59, 2398–2402.

Fei123, 2017. Distribution of smog in Guangzhou: Comprehensive explanation of latest Chinese smog distribution in 2016. http://www.fei123.com/2020000/2018145.shtml,-06-30. (In Chinese)

Gossman D., 2011. Process compatible $SO_2$ control in cement kilns. http://gcisolutions.com/gcitn0711.html.

Hajat, S., Anderson, H.R., Atkinson, R.W., 2002. Effects of air pollution on general practitioner consultations for upper respiratory diseases in London. Occup. Environ. Med. 59, 294–299.

Hansen, J.P., Jensen, L.S., Wedel, S., Johansen, K.D., 2003. Decomposition and oxidation of pyrite in a fixed-bed reactor. Ind. Eng. Chem. Fundam. 42, 4290–4295.

Höhn, S., Frimmel, H.E., Debaille, V., Pašava, J., Kuulmann, L., Debouge, W., 2017. The case for metamorphic base metal mineralization: pyrite chemical, Cu and S isotope data from the Cu-Zn deposit at Kupferberg in Bavaria, Germany. Miner. Deposita. 52, 1145–1156.

Horkoss, S., 2008. Reducing the $SO_2$ emission from a cement kiln Int. J. Nat. Soc. Sci. 1, 7-15.

Hu G., 2007. Emission of $SO_2$ from cement production. Ph.D. Thesis, Technical University of Denmark.

Johansen, V., Christensen, N.H., 1979. Rate of formation of $C_3S$ in the system $CaO$-$SiO_2$-$Al_2O_3$-$Fe_2O_3$-$MgO$ with addition of $CaF_2$. Cem. Concr. Res. 9, 1–5.

Kacimi, L., Simon-Masseron, A., Ghomari, A., Derriche, Z., 2006. Influence of NaF, KF and $CaF_2$ addition on the clinker burning temperature and its properties. C.R. Chim. 9, 154–163.

Kamata, H., Ohara, H., Takahashi, K., Yukimura, A., Seo, Y., 2001. $SO_2$ oxidation over the $V_2O_5/TiO_2$ SCR catalyst. Catal. Lett. 73, 79–83.

Karstensen K H., 2012. Co-processing of alternative fuels and raw materials and treatment of organic h azardous wastes in the cement industry–International experiences. http://coprocessamento.org.br/cms/wp-content/uploads/2012/12/Coprocessamento_Kere_Helge_Karstensen.pdf

Kouhestani, H., Ghaderi, M., Large, R.R., Zaw, K., 2017. Texture and chemistry of pyrite at Chah Zard epithermal gold–silver deposit, Iran. Ore Geol. Rev. 84, 80–101.

Lapina, O.B., Balzhinimaev, B.S., Boghosian, S., Eriksen, K.M., Fehrmann, R., 1999. Progress on the mechanistic understanding of $SO_2$ oxidation catalysts. Catal. Today 51, 469–479.

Lee, B.E., Ha, E.H., Park, H.S. Kim, Y.J., Hong, Y.C., Lee, J.T., 2003. Exposure to air pollution during different gestational phases contributes to risks of low birth weight. Hum. Reprod.18, 638–643.

Lei, Y., Zhang, Q., Nielsen, C., 2011. An inventory of primary air pollutants and $CO_2$ emissions from cement production in China, 1990–2020. Atmos. Environ. 45, 147–154.

Li, X., Xu, W., Wang, S., Tang, M., Shen, X., 2014. Effect of $SO_3$ and MgO on Portland cement clinker: Formation of clinker phases and alite polymorphism. Constr. Build. Mater. 58, 182–192.

Ma, J., Liu, Z., Liu, Q., Guo, S., Huang, Z., Xiao, Y., 2008. $SO_2$ and NO removal from flue gas over $V_2O_5$/AC at lower temperatures-role of $V_2O_5$ on $SO_2$ removal. Fuel Process. Technol. 89, 242–248.

Ministry of Ecological and Environmental Protection of China (MEEPC), 2016. National Bulletin of Environment Statistics.

Mut, M.M.C., Nørskov, L. K., Frandsen, F. J., Glarborg, P., 2015. Review: Circulation of inorganic elements in combustion of alternative fuels in cement plants. Energ. Fuel. 29, 4076–4099.

Oliveira, M.L.S., Waanders, F., Silva, L.F.O., Jasper, A., Sampaio. C.H., McHabe, D., Hatch, R.S., Hower, J.C., 2011. A multi-analytical approach to understand the chemistry of Fe-minerals in feed coals and ashes. Coal Comb. Gasif. Prod. 3, 51–62.

Ostwald, J., England, B.M., 1979. The relationship between euhedral and framboidal pyrite in base-metal sulphide ores. Miner. Mag. 43, 297–300.

Pourghahramani, P., Akhgar, B.N., 2015. Characterization of structural changes of mechanically activated natural pyrite using XRD line profile analysis. Int. J. Miner. Process. 134, 23–28.

Rasmussen, M.H., 2012. Low $SO_2$ emission preheaters for cement production. Ph.D. Thesis, Technical University of Denmark.

Sawlowicz, Z., 1993. Pyrite framboids and their development: a new conceptual mechanism. Geol Rundsch. 82, 148–156.

Shen, W., Liu, Y., Yan, B., Wang, J., He, P., Zhou, C., Huo, X., Zhang, W., Xu, G., Ding, Q., 2017. Cement industry of China: Driving force, environment impact and sustainable development. Renew. Sust. Energ. Rev. 75, 618–628.

Shi, M., Hung, J., Wang, T., Lin, R., 2004. Kinetics of the reaction of sulfur dioxide with calcium oxide powder. J. Chin. Inst. Chem. Eng. 35, 447–454.

Shih, S.M., Hung, J.T., Wang, T.Y., Lin, R.B., 2004. Kinetics of the reaction of sulfur dioxide with calcium oxide powder. J. Chin. Inst. Chem. Eng. 35, 447–454.

Tang, X., Jiang, Z., Jiang, S., Li, Z., Peng, Y., Xiao, D., Xing, F., 2018. Effects of organic matter and mineral compositions on pore structures of shales: A comparative study of lacustrine shale in Ordos Basin and Marine Shale in Sichuan Basin, China. Energy Explor. Exploit 36, 28–42.

Vlisidis, A.C., 1966. The determination of sulfate and sulfide sulfur in rocks or minerals. US Government Printing Office, Washington.

Wang, L., Wang, J., Xu, P., Li, Q., Zhang, W., Cui, S., 2015. Selectivity of transition metal catalysts in promoting the oxidation of solid sulfites in flue gas desulfurization. Appl. Catal. A-Gen. 508, 52–60.

Wells, J.J., Wigley, F., Foster, D.J., Livingston, W.R., Gibb, W.H., Williamson, J., 2005. The nature of mineral matter in a coal and the effects on erosive and abrasive behavior. Fuel Process. Technol. 86, 535–550.

Xiao, L., Zhao, B., Duan, P., Shi, Z., Ma, J., Lin, M., 2016. Geochemical Characteristics of Trace Elements in the No. 6 Coal Seam from the Chuancaogedan Mine. Jungar Coalfield, Inner Mongolia, China. Miner. 6, 1–14.

Xie, P., Song, H., Wei, J., Li, Q., 2016. Mineralogical characteristics of Late Permian Coals from the Yueliangtian coal mine. Guizhou, Southwestern China. Miner. 29, 1–21.

Zhang, S., Worrell, E., Crijns-Graus, W., 2015. Evaluating co-benefits of energy efficiency and air pollution abatement in China's cement industry. Appl. Energ. 147, 192–213.

**Highlights:**

1. 80 high-$SO_2$ emission NSP cement lines in China were investigated.

2. The pyrite morphology, sulfur content and species of limestones were analyzed.

3. The sulfur characteristics of limestones were correlated to their $SO_2$ emissions.

4. The sulfur flow, $SO_2$ release and capture in a NSP cement line were established.

5. Factors influencing the $SO_2$ emission of NSP cement line were discussed.